Showcasing a study on the thermodynamic and kinetic properties of $Na_xFe(SO_4)_2$ ($x = 0-2$): toward a high-capacity and low-cost cathode material by Amitava Banerjee, Rafael B. Araujo and Prof. Rajeev Ahuja at the Matter Theory Division, Department of Physics and Astronomy, Uppsala University, Sweden.

Unveiling the thermodynamic and kinetic properties of $Na_xFe(SO_4)_2$ ($x = 0-2$): toward a high-capacity and low-cost cathode material

New kinds of eldfellite materials are discovered to obtain higher capacity by *ab initio* quantum mechanical calculations. Moreover, the phase stability, electrochemical properties and ionic diffusion are also investigated to unveil the thermodynamic and kinetic properties of eldfellite materials.

ROYAL SOCIETY
OF CHEMISTRY

www.rsc.org/MaterialsA

PAPER

Unveiling the thermodynamic and kinetic properties of $Na_xFe(SO_4)_2$ ($x = 0-2$): toward a high-capacity and low-cost cathode material†

Amitava Banerjee,[*a] Rafael B. Araujo[*a] and Rajeev Ahuja[ab]

The mineral eldfellite, $NaFe(SO_4)_2$, was recently proposed as an inexpensive candidate for the next generation of cathode application in Na-based batteries. Employing the density functional theory framework, we have investigated the phase stability, electrochemical properties and ionic diffusion of this eldfellite cathode material. We showed that the crystal structure undergoes a volume shrinkage of $\approx 8\%$ upon full removal of Na ions with no imaginary frequencies at the Γ point of phonon dispersion. This evokes the stability of the host structure. According to this result, we proposed structural changes to get higher specific energy by inserting two Na ions per redox-active metal. Our calculations indicate $NaV(SO_4)_2$ as the best candidate with the capability of reversibly inserting two Na ions per redox center and producing an excellent specific energy. The main bottleneck for the application of eldfellite as a cathode is the high activation energies for the Na^+ ion hop, which can reach values even higher than 1 eV for the charged state. This effect produces a low ionic insertion rate.

1. Introduction

The Li-ion battery (LIB) has already proved its undoubted ubiquitousness in the portable electronics market.[1] Now to further drive out modern society from its fossil fuel dependency, it is crucial to expand its territory to large-scale electric energy storage applications, such as electric vehicles, smart grids, etc. But the main drawback of the lithium based rechargeable battery for large-scale application is the high cost of Li resources, which becomes a hindrance for industrial production. In this scenario, Na-ion batteries (SIB) emerge as a promising candidate for large-scale electric energy storage applications due to their low cost, uniform geographical distribution and the abundance of sodium resources. Therefore, sodium chemistry arises with a very wide range of possibilities to develop economically and environmentally friendly batteries for applications where energy density is not a concern.

The study of Na intercalation chemistry started from 1980, when, for instance, Na_xCoO_2 had been reported as a cathode material.[2–4] So far, various Na based compounds have been explored experimentally as well as theoretically as potential candidates for cathode application in SIBs. Some examples are $Na_2Fe_2(SO_4)_3$,[5] Na_2FePO_4F,[6] $Na_2FeP_2O_7$,[7] $Na_2Ni_2TeO_6$,[8] $Na_{2+2x}Mn_{2-x}(SO_4)_3$,[9] and $Na_2Fe(SO_4)_2 \cdot nH_2O$.[10] Most of these polyanions suffer from low theoretical capacity due to high molecular weight as well as low sodium insertion rate, limiting the battery performance. It is important that the selected cathode compound should deliver the highest possible potential together with good reaction rate, to have the greatest device performance.

Recently, P. Singh et al.[11] reported a low-cost cathode material, eldfellite ($NaFe(SO_4)_2$), with reversible sodium insertion capability at a voltage of 3.2 V versus Na/Na^+ for the Fe^{3+}/Fe^{2+} redox activity. This polyanion displayed a lower sodium insertion rate with a moderate specific energy. The specific energy can be tuned by doing structural modifications, which can allow for the full removal of Na ions from this compound. These modifications would produce a host that can insert two Na ions per redox active center, hence increasing the final specific energy of the material. Moreover, there needs to be an in-depth understanding of sodium insertion kinetics to propose a relevant mechanism for driving ionic diffusion into the eldfellite crystal structure. Thus, in the end, a fruitful strategy can be designed to increase the cell reaction kinetics.

In the present study, we are focusing on the theoretical capacity enhancement of this material by accessing the full desodiated state. Moreover, we aim to clarify what are the limiting factors to reach a faster sodium insertion rate during cell reaction. In this context, density functional theory formalism has been considered to determine the structural stability, charge transfers with sodium insertion, corresponding

[a]Condensed Matter Theory Group, Department of Physics and Astronomy, Uppsala University, Box 516, S-75120 Uppsala, Sweden. E-mail: amitava245@gmail.com

[b]Applied Materials Physics, Department of Materials and Engineering, Royal Institute of Technology (KTH), S-10044 Stockholm, Sweden

† Electronic supplementary information (ESI) available: The ground state structure of each composition of $Na_xFe(SO_4)_2$ ($x = 0-2$) obtained from the global optimization process is shown here. See DOI: 10.1039/c6ta05330k

17960 | J. Mater. Chem. A, 2016, 4, 17960–17969

This journal is © The Royal Society of Chemistry 2016

average redox potential, and ionic diffusion in the new Eldfellite ($NaFe(SO_4)_2$).

2. Computational details

Electronic structure calculations have been carried out with the density functional theory (DFT) framework based on the projector augmented wave method (PAW) as implanted in the Vienna Ab initio Simulation Package (VASP).[12,13] The Perdew, Burke, and Ernzerhof (PBE) parameterization for the exchange and correlation functional was used in an all spin polarized calculation.[14] We have also considered the GGA + U approach as implemented by Dudarev *et al.*,[15] to partially nullify the self-interaction error of standard DFT and also to include the strong correlation of the 3d electrons of the transition metal. In this level of theory an effective U value, *i.e.* $U_{eff} = U - J$ was considered, instead of separately considering the Hubbard repulsion term U and the exchange term J (where $J = 1$ eV). The U parameter (hereafter $U_{eff} = U$) of Fe was taken as 4 eV in this study.[16] A super-cell with 16 formula units was considered to study the thermodynamic properties. Energy minimization calculations have been carried out at a single Γ k-mesh and with an energy cut off for the plane-waves of 500 eV. Then, the electronic structures were evaluated with a finer $2 \times 2 \times 2$ grid. Ferromagnetic ordering was applied in most of the calculations.

To get an in-depth understanding of the sodium intercalation and extraction process, different sodium concentrations for $Na_xFe(SO_4)_2$ ($x = 0$–2) were explored by varying x at an interval of 0.25. All compositions were globally optimized with a basin-hopping Monte Carlo algorithm by considering more than 300 structures in each case.[17]

To investigate the ionic transport properties, *ab initio* molecular dynamics (AIMD) simulations were performed in conjunction with the climbing nudged elastic band method (cNEB).[18,19] In this part of the investigation, a supercell containing 16 formula units was used with the number of atoms varying from 208 to 191 atoms for $Na_2Fe(SO_4)_2$ and $NaFe(SO_4)_2$, respectively. Due to the large size of the supercell, these calculations were carried out with a single Γ centered k-mesh. For the cNEB calculations, the plane waves were expanded in an energy cut-off of 500 eV. For the AIMD, non-spin polarization was considered, and the cut-off was lowered to 400 eV.

The AIMD simulations were performed with a time step of 2 fs producing a sample equilibration of 50 ps for analysis of the diffusion properties. The first 10 ps were used to allow the system to reach the desired geometry and equilibrate with the required temperature. Then, they were discarded for the subsequent simulation. Temperatures varying from 900, 1000, 1100, 1200, 1300 and 1500 K were considered in the canonical ensemble (fixed particle number, volume, and temperature, NVT). These temperatures were chosen to accelerate the dynamic process. The mean squared displacement (MSD) and the atomic trajectories are the two-target information to be investigated. Then, with the MSD, the Einstein relation can derive diffusion coefficients as described in ref. 20 and 21. Moreover, from the atomic trajectories, it is possible to have good insight of the most favourable pathways for ionic diffusion.

The activation energies were computed by applying the cNEB framework. For each considered migration path, 4 or 5 images were linearly interpolated between the two equilibrium sites. Moreover, geometries were converged when forces in each atom were smaller than 2 meV Å^{-1}.

The stability of the fully desodiated phase was studied by considering two different approaches: firstly, we computed the phonon dispersion with a finite displacement approach, considering a super cell of 16 formula units. Secondly, an AIMD simulation at 1000 K was performed with a 40 ps time scale, using the same strategy as explained above. The main idea was to find any broken bonds during the simulation.

3. Results & discussions

Eldfellite stabilizes within the monoclinic prismatic crystal class having a space group $C2/m$ as is depicted in Fig. 1(b). In this structure, it has been observed that the Na^+ and Fe^{3+} cations are arranged in a different ab plane and alternatively propagated along the c direction. The six-oxygen coordinated Fe-polyhedra, FeO_6, are linked with the neighbouring SO_4 tetrahedra by their shared polyhedral vertex oxygen atom. Therefore each FeO_6 octahedra is connected with six SO_4 tetrahedra. These tetrahedra are orientated in a pinwheel pattern when observed along the b-axis (as is shown in Fig. 1(b)), keeping the FeO_6 polyhedra as a centre. Whereas each SO_4 tetrahedron is surrounded by three FeO_6 octahedra and the fourth unshared corner oxygen of this tetrahedra is pointing towards an open channel where Na atoms can sit.

The lattice parameters of $NaFe(SO_4)_2$ are shown in Table 1, which are within the negligible discrepancies of the experimentally reported ones.[22] The slight overestimation of the values is within the well-known trend of the PBE functional.

The ground state structure of each composition obtained from the global optimization process is identified and shown in Fig. S1.† Then, the formation energies of these configurations are calculated by the following equation:

$$E_f = E_{Na_xFe(SO_4)_2} - \left[\frac{xE_{Na_2Fe(SO_4)_2} + (2-x)E_{Fe(SO_4)_2}}{2} \right] \quad (1)$$

where $E_{Na_xFe(SO_4)_2}$ is the calculated energy of a particular composition with a corresponding x, varying from 0 to 2.

Ultimately the most stable ground state configuration is obtained by computing the formation energy with respect to two end structures, *i.e.*, $Fe(SO_4)_2$ and $Na_2Fe(SO_4)_2$, as represented in eqn (1). The only structure that lies on the convex hull lines is $NaFe(SO_4)_2$ which would produce a voltage profile with two plateaus during the cell reaction. Moreover, $Fe(SO_4)_2$ did not show any negative frequency at the Γ point of phonon dispersion, which evokes the dynamical stability of this structure. It is noticeable that full sodium extraction is possible for this structure without affecting the dynamical stability, which can allow higher capacity to be obtained.

It has been observed that the fully desodiated phase ($Fe(SO_4)_2$) and sodiated phase ($Na_2Fe(SO_4)_2$) have similar crystal

This journal is © The Royal Society of Chemistry 2016
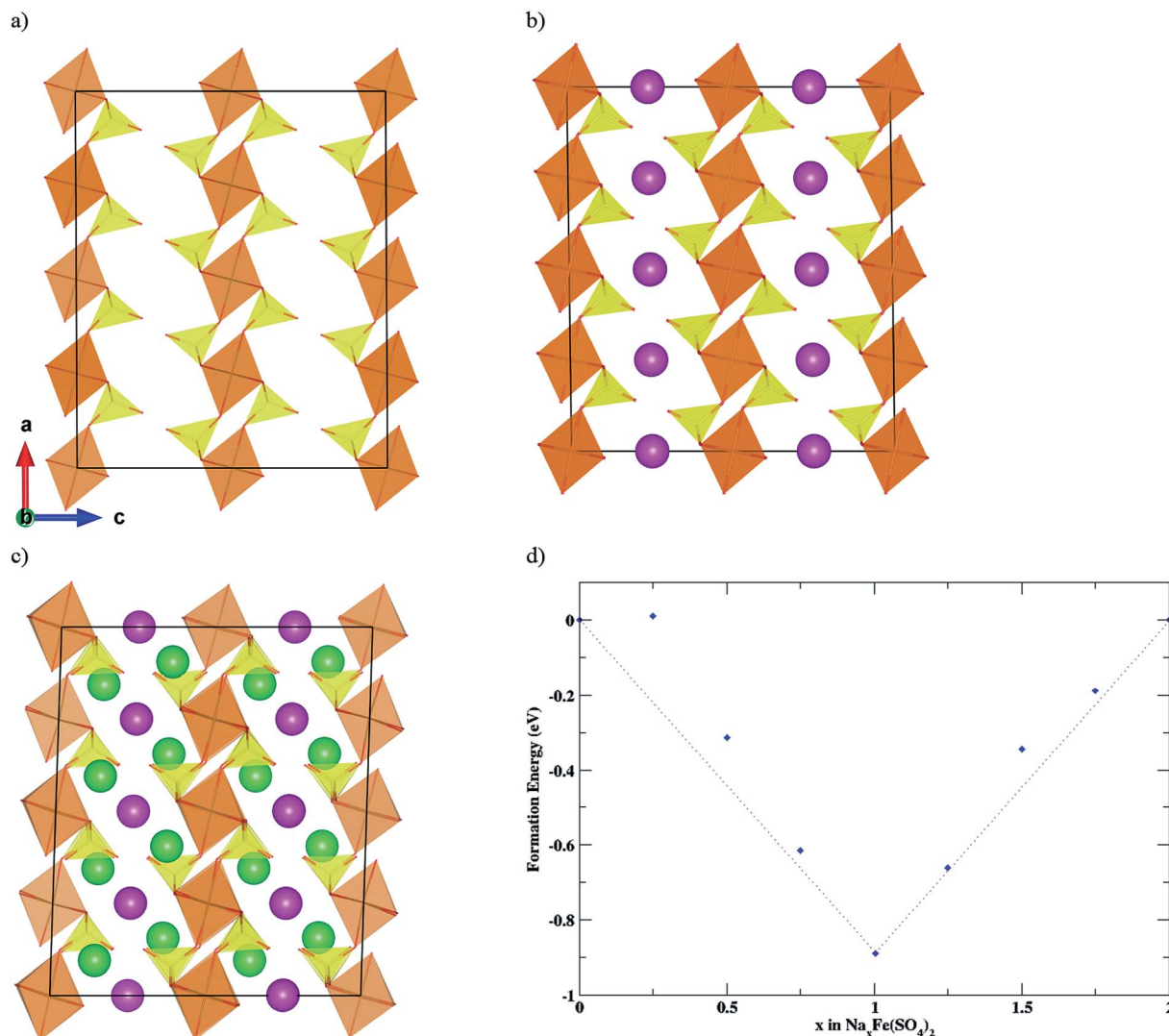
J. Mater. Chem. A, 2016, **4**, 17960–17969 | **17961**

Fig. 1 Crystal structure of (a) $Fe(SO_4)_2$, (b) $NaFe(SO_4)_2$ and (c) $Na_2Fe(SO_4)_2$. (d) Convex hull plot of the formation energy with compositions. In this case, the sodium concentration varies from 0 to 2 per formula unit. The brown polyhedra stand for Fe-polyhedra, the yellow polyhedra stand for the sulphur polyhedra, the violet colour atoms stand for Na1 and the green colour atoms stand for Na2.

Table 1 Optimized lattice parameters and cell volume of the cathode materials

Compound	a (Å)	b (Å)	c (Å)	α (°)	β (°)	γ (°)	Cell volume (Å^3)
$Na_2Fe(SO_4)_2$	8.50	5.46	7.17	89.99	88.14	90.01	332.87
$NaFe(SO_4)_2$	8.12	5.23	7.19	90.00	90.75	90.00	305.66
	8.04^a	5.14^a	7.11^a				
$Fe(SO_4)_2$	8.38	5.30	6.94	89.99	90.29	89.99	307.01

^{a} X-ray powder diffraction data.[22]

Table 2 Calculated average bond length, polyhedral volume and polyhedral distortion coefficient of the cathode material

Compound	Bond	Bond length (Å)	Polyhedral volume (Å^3)	Distortion coefficient
$Na_2Fe(SO_4)_2$	Fe–O	2.167	13.452	0.032
	S–O	1.495	1.709	0.011
$NaFe(SO_4)_2$	Fe–O	2.005	10.990	0.018
	S–O	1.482	1.692	0.014
$Fe(SO_4)_2$	Fe–O	2.002	10.876	0.014
	S–O	1.480	1.678	0.012

symmetry $C2/m$. However, in the case of $Na_2Fe(SO_4)_2$ the octahedra are tilted. Due to the insertion of the Na2 ions (represented by the green spheres in Fig. 1(c)), the S–O^u bonds are pushed (unshared oxygen of the tetrahedra is denoted as O^u) in the opposite direction to the 'a' axis. This atomic rearrangement

alters the bond angle of O–S–O^u from 111.5° to 113.9°, causing a rotation of the SO_4 tetrahedra along the b axis and finally rotating the FeO_6 octahedra. Still each FeO_6 octahedra is linked with six SO_4 tetrahedra as in $NaFe(SO_4)_2$, and the fourth unshared oxygen pointed towards the sodium channel.
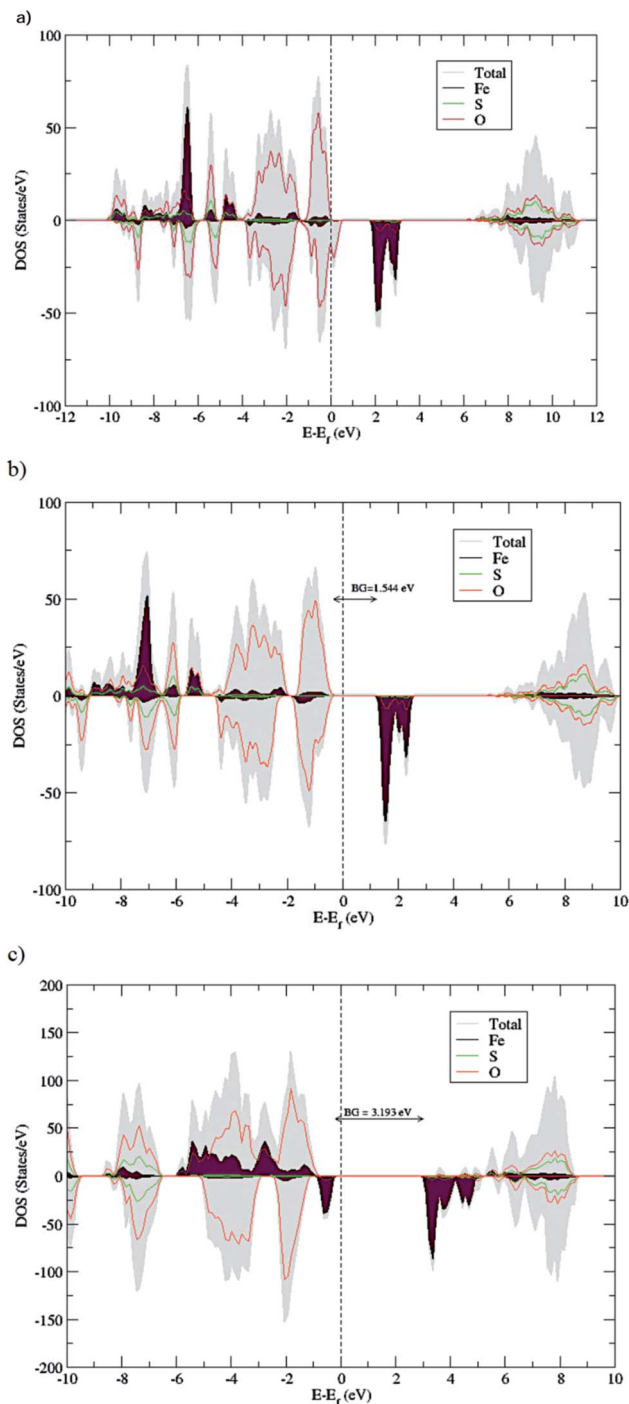
Fig. 3 Cell voltage variation with transition metal (M) substitution, where M = Co, Cr, Cu, Mn, Ni, Ti, V, and Fe.

Table 3 Average net Bader charge of the ground states of Na_2-$Fe(SO_4)_2$, $NaFe(SO_4)_2$ and $Fe(SO_4)_2$

Compound	Na	Fe	S	O
$Na_2Fe(SO_4)_2$	+0.85	+1.48	+3.76	−1.33
$NaFe(SO_4)_2$	+0.87	+1.85	+3.82	−1.29
$Fe(SO_4)_2$		+1.87	+3.77	−1.18

Fig. 2 Projected density of states of (a) $Fe(SO_4)_2$, (b) $NaFe(SO_4)_2$ and (c) $Na_2Fe(SO_4)_2$. The grey background in each plot shows the total density of states.

The insertion of sodium ions into the $NaFe(SO_4)_2$ crystal structure distributed the Na^+ in different sites, as is depicted in Fig. 1(c), where the green spheres represent the newly inserted Na ions at position Na2 and the violet spheres represent the previously presented Na ions at position Na1. Along the b-direction, the Na2 positions looks like they are sandwiching the previous sodium layer, Na1.
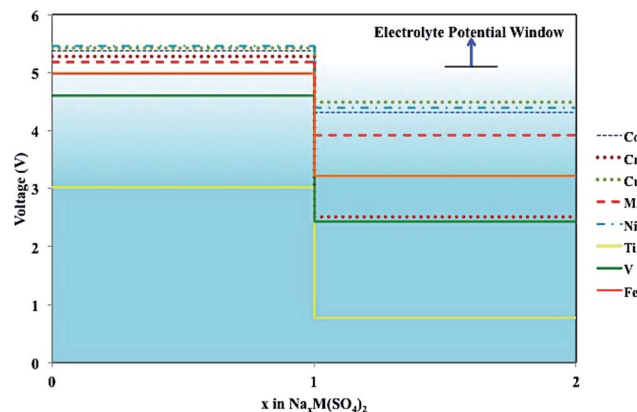
Whereas in the desodiated phase ($Fe(SO_4)_2$), both polyhedra (*i.e.* the octahedra and tetrahedra) arranged in a similar pinwheel fashion to $NaFe(SO_4)_2$. The noticeable difference with the $NaFe(SO_4)_2$ structure is the change of the lattice parameter and volume as is shown in Table 1.

From the fully sodiated phase to the half sodiated phase, the cell volume decreases on the order of 8.17%. Then, the cell volume again expands around ∼0.18% from the half sodiated phase to the fully desodiated phase. We can infer that the cell volume changes with a polyhedral volume change. It is quite noticeable from Table 2 that from the fully sodiated phase to the half sodiated phase ($Na_2Fe(SO_4)_2 \rightarrow NaFe(SO_4)_2$) the volume of the octahedra and tetrahedra decreases on the order of 18.28% and 0.76%, respectively. Whereas from the half sodiated phase to the fully desodiated phase again both polyhedra volumes decrease, on the order of 1.03% and 0.83% for the FeO_6 octahedra and SO_4 tetrahedra, respectively. This reflects the small cell volume change in this part of the reaction. From the above analysis, it is justifiable that the volume change of the FeO_6 octahedra is the main key factor for the total cell volume change. Consequently, the change in the Fe–O bond length influences this octahedra volume change and also the octahedral distortion. In the case of the first Fe oxidation, from the fully sodiated phase to the half sodiated phase the Fe–O bond length decreases, which is due to oxidation occurring on the transition metal center. This bond length variation with the oxidation process is also reported in the case of $Na_2Fe_2(SO_4)_3$.[23] At the same time, it is interesting to observe that during the second removal of Na^+ ions, the Fe–O bond length decrease is negligible. This different feature could be because the oxidation

Table 4 Calculated cell voltage, cell volume change and specific energy with transition metal substitution

Compound	Cell voltage (V)		Cell volume change (%)		Specific energy (W h kg^{-1})	
	Na2 to Na1	Na1 to Na0	ΔVol_{2-1}	ΔVol_{1-0}	Na2 to Na1	Na1 to Na0
Ti(SO$_4$)$_2$	0.77	3.02	7.61	0.65	72.19	307.93
V(SO$_4$)$_2$	2.42	4.61	8.21	2.71	224.50	464.62
Cr(SO$_4$)$_2$	2.51	5.27	12.20	1.36	232.01	529.05
Mn(SO$_4$)$_2$	3.91	5.17	10.40	0.37	357.78	513.36
Fe(SO$_4$)$_2$	3.21	4.98	8.17	0.18	292.82	493.82
Co(SO$_4$)$_2$	4.31	5.38	8.34	−0.36	389.07	526.41
Ni(SO$_4$)$_2$	4.39	5.45	5.99	−2.34	396.62	533.73
Cu(SO$_4$)$_2$	4.48	5.42	10.13	−0.67	398.24	521.55

process does not occur on Fe sites. Bader charge analysis is used to explain this trend in the following paragraphs.

The average intercalation potential *vs.* Na/Na$^+$ is theoretically computed by the DFT framework, under consideration of this general cell reaction:

$$(x - x_0)Na^+ + (x - x_0)e^- + Na_{x_0}M(SO_4)_2 \rightarrow Na_xM(SO_4)_2$$
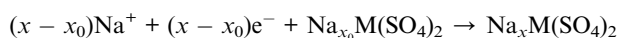
where M is the transition metal center, which is Fe in this case. In the case of the first sodium intercalation, $x = 1$ and $x_0 = 0$, and the reacting materials are NaFe(SO$_4$)$_2$ and Fe(SO$_4$)$_2$. For the second intercalation process $x = 2$ and $x_0 = 1$, and the participating redox materials are Na$_2$Fe(SO$_4$)$_2$ and NaFe(SO$_4$)$_2$. The average intercalation potential is calculated by taking the ground state energy difference in between the desodiated and sodiated phases, by using the following equation:[24]

$$V = -\left[\frac{E_{Na_xM(SO_4)_2} - (x - x_0)E_{Na} - E_{Na_{x_0}M(SO_4)_2}}{(x - x_0)}\right] \quad (2)$$

where E is the ground state energy of the corresponding system. Fig. 3 displays the computed average redox potential *vs.* Na/Na$^+$. It has been observed that in the first plateau of the voltage profile, where the NaFe(SO$_4$)$_2$ and Na$_2$Fe(SO$_4$)$_2$ compounds are involved in the reaction, the computed redox potential is 3.21 V. This intercalation potential value shows a sensible agreement with the reported experimental value of ≈3.2 V.[11] In the case of the second step of the reaction, where the sodium ions are removed from NaFe(SO$_4$)$_2$ to form Fe(SO$_4$)$_2$, the computed redox potential is 4.98 V. Although the second plateau winds up with a greater redox potential, it is still inside the potential window of the electrolyte.[25,26] It has been observed, from vibrational frequency analysis, that the Fe(SO$_4$)$_2$ phase is dynamically stable. Again, after running the AIMD simulation for 40 ps at 1000 K, we have not observed any broken bonds, also indicating the high degree of stability of Fe(SO$_4$)$_2$. Therefore, from a thermodynamics point of view, it is possible to achieve the full desodiation phase without any structural phase change, as well as with a fruitful redox potential that lies inside the electrolyte potential window. Hence, it is quite profitable to remove all sodium to get a higher capacity.

The total density of state (DOS) and the projected density of state (pDOS) of Na$_x$Fe(SO$_4$)$_2$ (where $x = 0, 1, 2$) are shown in

Fig. 2. A transition from half-metallic to semiconductor with the insertion of Na ions in the Fe(SO$_4$)$_2$ crystal structure is depicted. On the other hand, there is an increasing trend in band gap from 1.54 eV to 3.19 eV from the half sodiated compound to the fully sodiated compound, respectively. From the pDOS, it has been observed that the S atoms are mainly contributing to the density of state below −5 eV. Below this energy level, the contribution is also imparted by the hybridization between the S and O atomic states, which further implies the formation of the strong S–O covalent bond by lowering the states far below the Fermi level, whereas the Fe-d state and the O-p state are stretched out throughout the pDOS. It has also been observed that the valance band edge and conduction band edge are mostly contributed from the O-p and Fe-d orbitals. It is quite noticeable that, in the case of NaFe(SO$_4$)$_2$, the valance band edge is mostly constructed by states of O-p whereas in the case of Na$_2$Fe(SO$_4$)$_2$ it is constructed by Fe-d states. For the fully desodiated case, a strong contribution of O is depicted which crosses the Fermi level and signifies the half metallicity of Fe(SO$_4$)$_2$. This higher contribution of O-p instead of Fe-d at the Fermi level implies that the oxidation process takes place on the O center instead of the Fe center of Fe(SO$_4$)$_2$. It is important to highlight that the transition between the half-metallic state to the semiconductor state upon sodium insertion will not be observed. In fact, the Curie temperature of these compounds is much lower than the usual working temperature of the cell. To further confirm it, we have performed calculations on the antiferromagnetic state for the NaFe(SO$_4$)$_2$ compound. The displayed energetic difference between the material in the ferromagnetic and antiferromagnetic configuration goes to 0.02 eV. It confirms the small magnetic coupling resulting in a very small Curie temperature.

This phenomenon (oxidation on metal/non-metal center) can also be verified by comparing the magnetic moment. During the first desodiation process, the magnetization of the Fe center changes from 3.7 μ_B per atom to 4.3 μ_B per atom, respectively from Na$_2$Fe(SO$_4$)$_2$ to NaFe(SO$_4$)$_2$. This means that the oxidation process occurs on the Fe centers. In the second desodiation process there is no change in the magnetization of Fe, but the magnetization of O changes from 0.02 to 0.2 μ_B per atom. Therefore, it can be speculated that the extra electron transfer takes place on the p orbitals of the O atoms. It is also
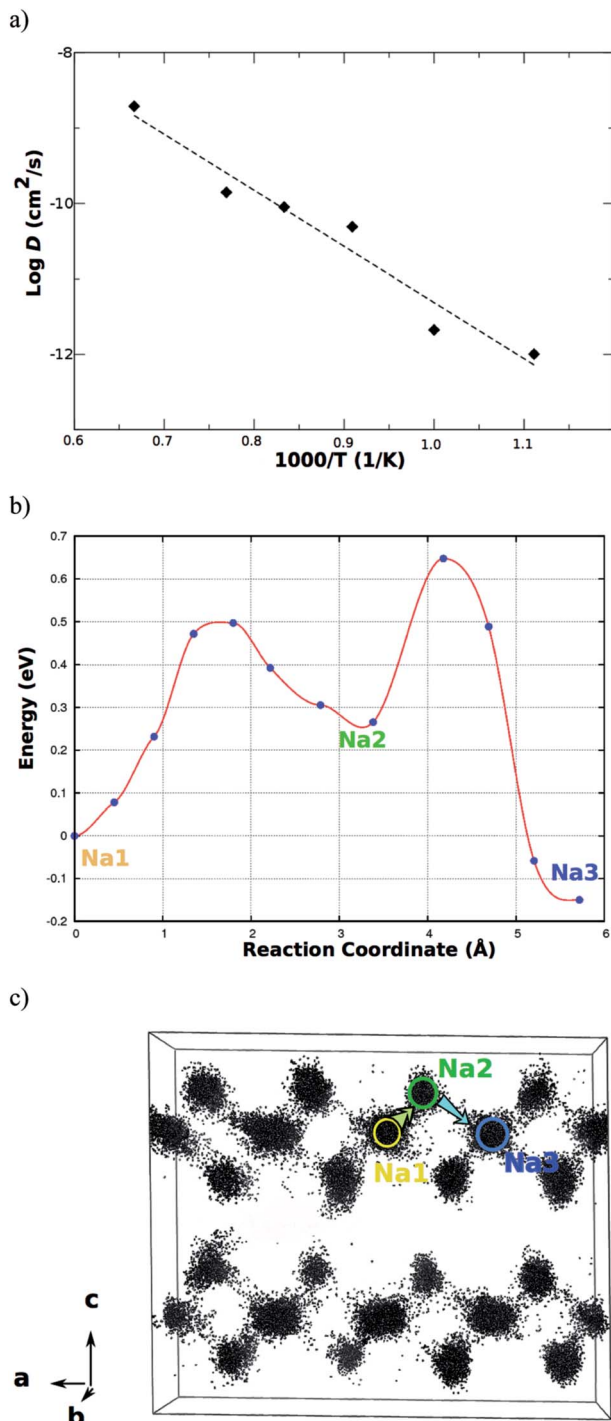
17964 | *J. Mater. Chem. A*, 2016, **4**, 17960–17969

This journal is © The Royal Society of Chemistry 2016

Fig. 4 (a) Arrhenius plot for $Na_2Fe(SO_4)_2$. (b) Energy profile computed with the cNEB method for the migration of Na ions from Na1–Na2 and Na2–Na3 in the $Na_2Fe(SO_4)_2$ crystal structure. (c) Na ion trajectories over the simulated time scale at 1500 K.

observed that the change in magnetization is mainly on the unshared O of the SO_4 tetrahedra.

The in-detail scenario of this charge transfer process can be viewed from the Bader analysis. In this work the transfer process is evaluated in terms of net charge per atom, which is defined as the difference between the Bader charge and total

nuclear charge of that atom. It has been observed, from Table 3, that the charges for Na and S are more or less similar throughout the reaction cycle. There is a slight variation of charge from +3.76 to +3.82 and from −1.33 to −1.29, respectively on the S and O atom. On the basis of ionic bonding, oxygen should have a −2 atomic charge. However, the hybridization of the S and O states, as observed in the DOS, produces that variation of effective charge on S and O. After the half-desodiation process there is a negligible change in the effective charge of Na. Whereas in this process, the Fe center shows a noticeable variation of net Bader charge, from +1.48 to +1.85 per atom. This suggests that the redox reaction mostly takes place on the Fe center. The most interesting observation occurs during the full desodiation process, where there is almost no change in the net Bader charge of the Fe centers, but the net charges of the O atoms show a variation from −1.18 to −1.29. This again confirms that the redox reaction for the half desodiated phase to the fully desodiated phase occurs on the O atom of the SO_4 tetrahedra.

It has been observed in Fig. 3, as well as in the previous discussion, that for extracting two sodium atoms from the Fe-based system, a potential energy very close to the electrolyte stability potential window is needed. In terms of the efficient workability of the battery, it is always advisable to have the cell voltage below the electrolyte stability window with consideration of the appropriate specific energy. On this point of view, this study also reflects the effect of transition metal substitution on the cell voltage, cell volume and specific energy, as is shown in Table 4.

The half-desodiation process for all transition metal substitution shows, in general, an increasing trend of cell voltage with increasing atomic number of transition metal center. In the case of the full desodiation process, the change in cell voltage is quite anomalous. For instance, the predicted redox potentials from the Ti to Cr based systems show an increasing value with increasing atomic number. Suddenly, the Fe based polyanion comes up with a cell voltage smaller than the Mn based compound. Usually, polyanions formed with early transition metals such as V, Ti and Cr can reach greater oxidation states. Then, they are most likely to insert two Na ions reversibly into the crystal framework without involving O-p states in the reaction. On the other hand, compounds formed with Fe, Mn, Co or Ni tend to show difficulties oxidizing to the +4 state, resulting in a large involvement of O states upon full desodiation. The anomalous trend observed upon full desodiation is then explained through these features of the used transition metals.

From Table 4, by looking at only the cell voltage, the substitution of Ti and V is more acceptable since these two compounds deliver redox potential values smaller than 5 V under 2 Na insertion. However, at the same time, the Ti-based system shows a very low specific energy for the transition from the +2 to +3 oxidation state, as compared to all other substitutions. Therefore, V substitution comes up as the most promising candidate to finally have reversible two Na ion insertion per redox-center. This compound must produce a theoretical specific energy of the order of 689 W h kg^{-1}, which is higher than that of the currently used cathode $LiFePO_4$ (440 W h kg^{-1}).[27]
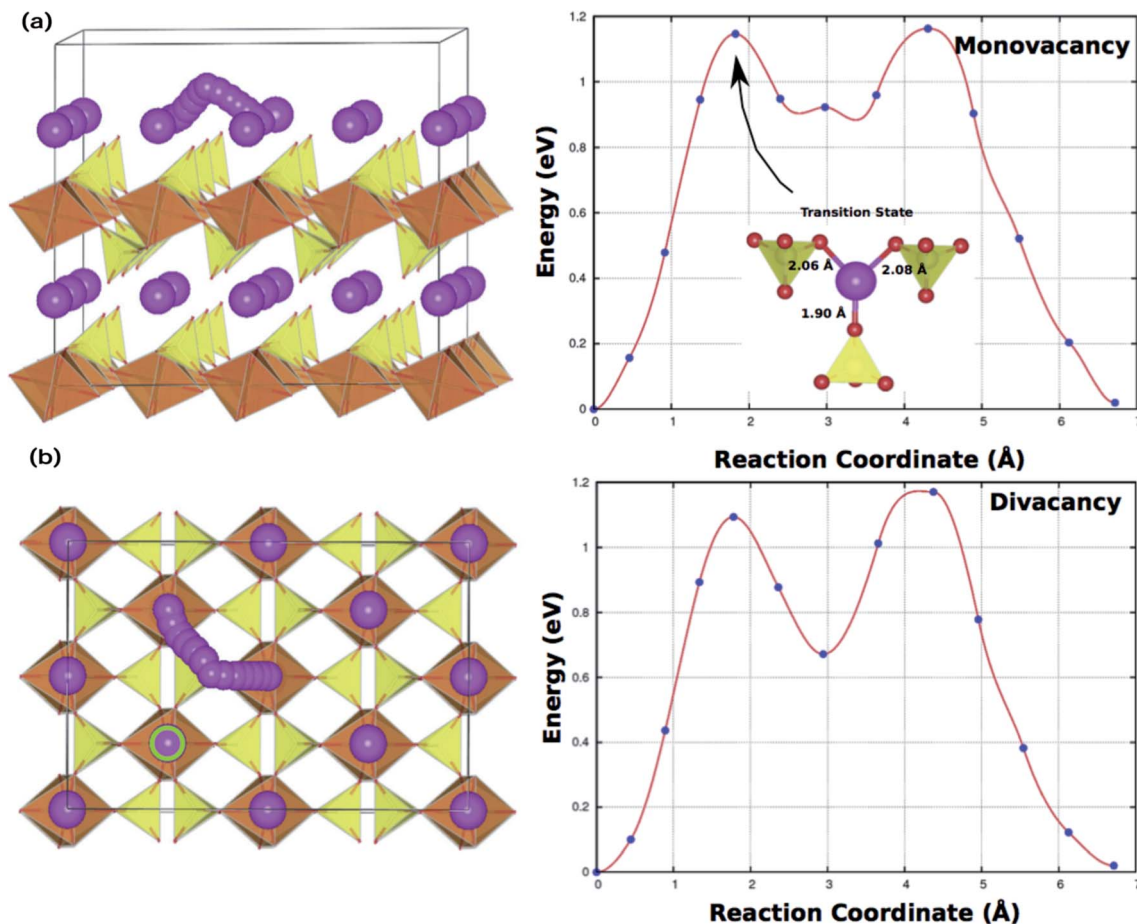
Fig. 5 Energy profile for the Na ion migration. Two possibilities were considered (a) monovacancy diffusion mechanism and (b) bivacancy diffusion mechanism.

From the several substitutions presented in Table 4, only two cases, V and Ti substitution, are inside the boundary condition of 5 V (*i.e.* electrolyte stability window) for the 2 electron reaction. On the other hand, it is still possible to increase the specific energy by only increasing the redox potential of the reaction concerning the oxidation state change from +2 to +3. The compounds containing Mn, Co, Ni or Cu show a redox potential that is much higher than the Fe-based compound. Moreover, for the Ni case the volumetric change is even smaller than that of the Fe-based compound. Therefore, even without activating a "two" ion insertion reaction, it is still possible to produce an eldfellite type material with greater specific energy than the one presented by $NaFe(SO_4)_2$.

Above all, reaction kinetics is also one of the important factors to be considered. For a comparative case study, we have selected the V-substituted system, since it has a quite reasonable cell voltage, volume change and also very high specific energy. The cell kinetics of this substituted system are discussed in comparison to the Fe-based system in the following section.

With AIMD simulation, it is possible to obtain the most probable ionic migration mechanism and the most frequented lattice positions over the simulation time scale displayed by the sodium atoms.

Fig. 4(c) depicts the trajectories of the sodium atoms during AIMD. These paths suggest that the diffusion of sodium ions is mostly happening in between the planes formed by the S–Fe–S polyhedra in the $Na_2Fe(SO_4)_2$ crystal structure. In fact, it is not surprising that the sodium atoms are likely to migrate in between these layers since there is no real space to cross them and, therefore, the electrostatic repulsion coming from the Fe and S atoms must result in high activation energies for the concerning pathway. The Na trajectories reveal the primary diffusion mechanism that occurs by hops between the Na1 positions to the Na2 positions. Then, when the ion is at the Na2 position, it can come back to Na1 or even move to a Na3 position, as is shown in Fig. 4(c). It is important to highlight that Na1 and Na3 are treated as nonequivalent positions due to some degree of disorder in the Na$^+$/vacancy arrangement.

The Arrhenius plot for diffusion coefficients at temperatures of 900, 1000, 1100, 1200, 1300 and 1500 K for Na$^+$ diffusion is shown in Fig. 4(a). From the slope of this plot it is possible to estimate the activation energy by the Arrhenius relation:[28]

$$D = A \ \exp\left(-\frac{E_a}{K_b T}\right) \tag{3}$$

17966 | *J. Mater. Chem. A*, 2016, **4**, 17960–17969

This journal is © The Royal Society of Chemistry 2016

where D is the diffusion coefficient and E_a is the activation energy barrier. Here, E_a is 0.58 eV, which is needed for Na mobility in this material.

To have a better insight into the dependency of the diffusion process with the local Na configuration, the energy barriers for the hop from Na1 to Na2 and Na2 to Na3 have been computed by using the cNEB framework. The activation energy for the hop from Na1 to Na2 displays a value of 0.49 eV, whereas the reverse process (Na2 → Na1) needs 0.24 eV, as is depicted in Fig. 4(b). At the second step, the migration of Na^+ from Na2 to Na3 and the opposite path shows a barrier of 0.39 eV and 0.80 eV, respectively.

The analysis of the activation energies from the cNEB together with the derived average activation energy from the molecular dynamics allows us to propose an ionic migration mechanism, where firstly, Na^+ ions hop from Na1 to Na2, and secondly, since there is no possibility to migrate through Na2 positions, the sodium ion migrates back to Na1 or forward to Na3. However, in both cases, at position Na1 and Na3, the next hop must experience an activation energy barrier in between 0.49 eV and 0.80 eV. Therefore, the paths Na1–Na2 and Na3–Na2 emerge as the rate-limiting steps for Na migration. Moreover, the average of the activation energies of these two processes is 0.64 eV which is slightly greater than the 0.58 eV derived from AIMD, hence supporting the proposed diffusion mechanism.

The possibility of ionic diffusion occurring through the layers is also investigated. The viability of this migration mechanism comes with the formation of anti-site defects, for instance, opening a space in the S–Fe–S polyhedral layers for the sodium migration. The calculation of the anti-site defect formation energy has followed the strategy described in ref. 9 with the same computational set up used for the cNEB calculation. The calculated formation energy is 2.69 eV. This high formation energy indicates the small probability of finding this kind of defect during the reaction. Consequently, it is very unlikely to have the migration of Na ions through the layers formed by S–Fe–S polyhedra.

The cNEB calculations have been carried out for the half-sodiated phase as well to draw a full picture of the diffusion process. Two different possibilities are analyzed here. Initially, a single sodium vacancy was created in the crystal structure of $NaFe(SO_4)_2$. Then, such as for the fully sodiated case, Na^+ is allowed to move from the Na1 position to the Na2 position, as is shown in Fig. 5(a). This pathway produces an activation energy barrier on the order of 1.15 eV.

Subsequently, the possibility of ionic migration influenced by divacancies taking place, as proposed by Van der Ven et al. in Li_xCoO_2,[29] is also investigated. Fig. 5(b) indicates, in the green color circle, the creation of the second vacancy and the activation energy for the ionic diffusion in the structure with two vacancies. The evaluated activation energy is on the order of 1.13 eV, which implies that the migration of Na^+ ions in $NaFe(SO_4)_2$ must not be mediated by divacancies.

With the assessment of both the migration mechanisms and the emerged activation energies for the Na^+ hop in $NaFe(SO_4)_2$, we can infer that, at the beginning of the charge reaction, the sodium insertion must suffer from a poor rate due to the high

activation energies. It is also shown that the main difference in the energy profile for the divacancy and monovacancy energy barriers appears in the Na2 site with quite distinct formation energies. This difference is an effect of the Na–Na interaction that is lowered when the divacancy is created stabilizing the Na2 site. Moreover, it is possible to speculate that the main responsible factor for the significant activation energy of the Na hop in the half sodiated phase must not be the Na–Na interaction since similar results are produced with distinct local Na environments (monovacancy and divacancy).

The investigation of thermodynamics on the eldfellite host showed that replacing Fe ions by V ions provides a way of increasing the specific energy by raising the voltage window. In this spirit, cNEB calculations have been performed for the Na^+ single vacancy migration in $NaV(SO_4)_2$ following the same pathways and procedure as in the case of the Fe based system. The derived activation energy is 1.18 eV with almost the same value as for the iron case, 1.13 eV. This means that the substantial effect producing these great barriers for the Na^+ hop comes from another source that is not from the Fe–Na or V–Na interaction.

Indeed, when the Na^+ ion is at the transition state, the closest atoms are three oxygen atoms as is depicted in Fig. 5(a). Therefore, we can speculate that the high activation energies come from the interaction of the Na^+ ion in the transition state with the three closest oxygen atoms and their link with the SO_4 tetrahedral.

The main bottleneck to reach the full desodiation of $NaV(SO_4)_2$ seems to be the high activation energies for the Na^+ ion hop. At low Na concentration, $Na_{1-x}V(SO_4)_2$ with x between 1 and 0, the Na–Na interactions are reduced, increasing the Na^+/vacancy ordering. Van der Ven et al.[29] showed that high ionic order results in lower diffusivity in Li_xCoO_2. This idea also supports our findings in two ways. One is the explanation of good diffusivity in the sodiated phase, $Na_2Fe(SO_4)_2$, and the second is the low ionic diffusivity in $NaFe(SO_4)_2$. The system containing more sodium atoms presents some degree of Na^+/vacancy disorder. This increases the ionic diffusivity in $Na_2Fe(SO_4)_2$. The second observation is the possibility of producing a compound with mixed transition metal elements. This strategy could create some degree of disorder in the Na sublattice of the half sodiated compound, $NaFe(SO_4)_2$, hence increasing the diffusivity at low concentrations as discussed by Mo et al.[30] This method to generate high rate compounds is evidenced by the good performance of some layered mixed transition metal compounds.[30–32] Further investigations are then of the utmost importance to infer whether this method is efficient or not to improve the ionic diffusion rates in the reference cathode material.

4. Conclusions

We have used the framework of the density functional theory to unveil the electrochemical redox mechanism of the recently proposed $NaFe(SO_4)_2$. Our modeled structure successfully reproduces the cell voltage reported experimentally. The combination of a basin-hopping algorithm with DFT allowed us

This journal is © The Royal Society of Chemistry 2016

J. Mater. Chem. A, 2016, **4**, 17960–17969 | **17967**

to finally resolve the most stable position of the Na ions upon the cell reaction. Once the crystal framework of $Na_{2-x}Fe(SO_4)_2$ was determined, we have shown that the full desodiated material, $Fe(SO_4)_2$, is dynamically stable with no imaginary frequencies in the phonon dispersion. This opens the possibility of activating a two-electron reaction by fully removing sodium atoms, consequently increasing the specific energy of this compound. The evaluation of the redox potential showed that a full Na ion removal in an Fe-based polyanion delivers a potential of around 5 V. This value is close to the electrolyte window potential. Therefore, increasing the window potential in the compound with Fe as the transition metal must result in the oxidation of the electrolyte, perturbing the workflow of the cell. We have proposed strategies to tune the specific energy of eldfellite by substituting Fe with other transition metals. Finally, it is shown that V substitutions emerge as the best candidate for the two-sodium insertion reaction. Moreover, we have predicted a migration mechanism where Na ions hop in between the two Na lattice positions with an activation energy on the order of 1.15 eV in the charged state, $NaFe(SO_4)_2$. This high barrier to the ion mobility is obtained for the compound with V instead of Fe as well. Therefore, we have shown that the main bottleneck to reach a two sodium insertion reaction seems to be the high activation energies of the Na^+ ion hop. Mixed transition metal substitution could be one of the possible alternatives to overcome this bottleneck. However, further investigations on this topic are still necessary to finally confirm that this strategy would end up with an improved performance of the device.

Acknowledgements

References

1 J. Z. Yang, J. Zhang, M. C. W. Kintner-Meyer, X. Lu, D. Choi, J. P. Lemmon and J. Liu, Electrochemical energy storage for green grid, Chem. Rev., 2011, 111, 3577.

2 G. H. Newman and L. P. Klemann, Ambient Temperature Cycling of an Na -TiS₂ Cell, J. Electrochem. Soc., 1980, 127, 2097.

3 C. Delmas, J. J. Braconnier, C. Fouassier and P. Hagenmuller, Electrochemical intercalation of sodium in Na_xCoO_2 bronzes, Solid State Ionics, 1981, 4, 165.

4 L. W. Shacklette and T. R. Jow, A Rechargeable Cell Based on a Conductive Polymer/Metal Alloy Composite Electrode, J. Electrochem. Soc., 1989, 136, 1–5.

5 P. Barpanda, G. Oyama, S. Nishimura, S. Chung and A. Yamada, A 3.8 V earth-abundant sodium battery electrode, Nat. Commun., 2014, 5, 4358.

6 B. L. Ellis, W. R. M. Makahnouk, Y. Makimura, K. Toghill and L. F. Nazar, A multifunctional 3.5 V iron-based phosphate cathode for rechargeable batteries, Nat. Mater., 2007, 6, 749–753.

7 P. Barpandaa, T. Ye, S. Nishimura, S. Chung, Y. Yamadaa, M. Okubo, H. Zhoua and A. Yamada, Sodium iron pyrophosphate: a novel 3.0 V iron-based cathode for sodium-ion batteries, Electrochem. Commun., 2012, 24, 116–119.

8 A. Gupta, C. Buddie Mullins and J. B. Goodenough, $Na_2Ni_2TeO_6$: evaluation as a cathode for sodium battery, J. Power Sources, 2013, 243, 817–821.

9 R. B. Araujo, M. S. Islam, S. Chakraborty and R. Ahuja, Predicting electrochemical properties and ionic diffusion in $Na_{2+2x}Mn_{2-x}(SO_4)_3$: crafting a promising high voltage cathode material, J. Mater. Chem. A, 2016, 4, 451–457.

10 M. Reynaud, M. Ati, S. Boulineau, M. T. Sougrati, B. C. Melot, G. Rousse, J.-N. Chotard and J.-M. Tarascon, Bimetallic Sulfates $A_2M(SO_4)_2 \cdot nH_2O$ (A = Li, Na and M = Transition Metal): as New Attractive Electrode Materials for Li- and Na-Ion Batteries, ECS Trans., 2013, 50(24), 11–19.

11 P. Singh, K. Shiva, H. Celio and J. B. Goodenough, Eldfellite, $NaFe(SO_4)_2$: an intercalation cathode host for low-cost Na-ion batteries, Energy Environ. Sci., 2015, 8, 3000.

12 G. Kresse and J. Hafner, Ab initio molecular dynamics for liquid metals, Phys. Rev. B: Condens. Matter Mater. Phys., 1993, 47, 558.

13 G. Kresse and J. Hafner, Efficient iterative schemes for ab initio total-energy calculations using a plane-wave basis set, Phys. Rev. B: Condens. Matter Mater. Phys., 1996, 54, 11169.

14 J. P. Perdew, K. Burke and M. Ernzerhof, Generalized gradient approximation made simple, Phys. Rev. Lett., 1996, 77, 3865.

15 S. L. Dudarev, G. A. Botton, S. Y. Savrasov, C. J. Humphreys and A. P. Sutton, Electron-energy-loss spectra and the structural stability of nickel oxide: An LSDA + U study, Phys. Rev. B: Condens. Matter Mater. Phys., 1998, 57, 1505.

16 T. Mueller, G. Hautier, A. Jain and G. Ceder, Evaluation of tavorite-structured cathode materials for lithium-ion batteries using high-throughput computing, Chem. Mater., 2011, 23, 3854–3862.

17 D. J. Wales and H. A. Scheraga, Global optimization of clusters, crystals, and biomolecules, Science, 1999, 285, 1368.

18 H. Jonsson; G. Mills and K. W. Jacobsen, in Classical and Quantum Dynamics in Condensed Phased Simulations, ed. B. J. Berne, G. Ciccotti and D. F. Coker, World Scientic, River Edge, NJ, 1998, p. 385.

19 G. Henkelman and H. J. Jonsson, Improved tangent estimate in the nudged elastic band method for finding minimum energy paths and saddle points, Chem. Phys., 2000, 113, 9978.

20 Y. Mo, S. P. Ong and G. Ceder, First principles study of the $Li_{10}GeP_2S_{12}$ lithium super ionic conductor material, Chem. Mater., 2011, 24, 15.

21 S. P. Ong, Y. Mo, W. D. Richards, L. Miara, H. S. Lee and G. Ceder, Phase stability, electrochemical stability and ionic conductivity of the $Li_{10\pm1}MP_2X_{12}$ (M = Ge, Si, Sn, Al

or P, and X = O, S or Se) family of superionic conductors, *Energy Environ. Sci.*, 2013, **6**, 148.

22 T. Balić-Žunić, A. Garavelli, P. Acquafredda, E. Leonardsen and S. P. Jakobsson, Eldfellite, NaFe(SO$_4$)$_2$, a new fumarolic mineral from Eldfell volcano, *Mineral. Mag.*, 2009, **73**, 51–57.

23 R. B. Araujo, S. Chakraborty, P. Barpanda and R. Ahuja, Na$_2$M$_2$(SO$_4$)$_3$ (M = Fe, Mn, Co and Ni): towards high-voltage sodium battery applications, *Phys. Chem. Chem. Phys.*, 2016, **18**, 9658.

24 M. S. Islam and C. A. J. Fisher, Lithium and sodium battery cathode materials: computational insights into voltage, diffusion and nanostructural properties, *Chem. Soc. Rev.*, 2014, **43**, 185.

25 S. Kazemiabnavi, Z. Zhang, K. Thornton and S. Banerjee, Electrochemical Stability Window of Imidazolium-Based Ionic Liquids as Electrolytes for Lithium Batteries, *J. Phys. Chem. B*, 2016, **120**(25), 5691.

26 A. Bhide, J. Hofmann, A. Katharina Dürr, J. Janek and P. Adelhelm, Electrochemical stability of non-aqueous electrolytes for sodium-ion batteries and their compatibility with Na$_{0.7}$CoO$_2$, *Phys. Chem. Chem. Phys.*, 2014, **16**, 1987.

27 J. Liu, J. Wang, X. Yan, X. Zhang, G. Yang, A. F. Jalbout and R. Wang, Long-term cyclability of LiFePO$_4$/carbon composite cathode material for lithium-ion battery applications, *Electrochim. Acta*, 2009, **54**, 5656–5659.

28 P. M. Panchmatia, A. R. Armstrong, P. G. Bruce and M. S. Islam, Lithium-ion diffusion mechanisms in the battery anode material Li$_{1+x}$V$_{1-x}$O$_2$, *Phys. Chem. Chem. Phys.*, 2014, **16**(39), 21114–21118.

29 A. Van der Ven, G. Ceder and M. Asta, Tepesch, first-principles theory of ionic diffusion with nondilute carriers, *Phys. Rev. B: Condens. Matter Mater. Phys.*, 2001, **64**, 184307.

30 Y. Mo, S. P. Ong and G. Ceder, Insights into diffusion mechanisms in P2 layered oxide materials by first-principles calculations, *Chem. Mater.*, 2014, **26**(18), 5208–5214.

31 Z. Lu and J. R. Dahn, In Situ X-Ray Diffraction Study of P2 Na$_{2/3}$[Ni$_{1/3}$Mn$_{2/3}$]O$_2$, *J. Electrochem. Soc.*, 2001, **148**, A1225.

32 D. Carlier, J. H. Cheng, R. Berthelot, M. Guignard, M. Yoncheva, R. Stoyanova, B. J. Hwang and C. Delmas, The P2-Na$_{2/3}$Co$_{2/3}$Mn$_{1/3}$O$_2$ phase: structure, physical properties and electrochemical behavior as positive electrode in sodium battery, *Dalton Trans.*, 2011, 9306.

This journal is © The Royal Society of Chemistry 2016

J. Mater. Chem. A, 2016, **4**, 17960–17969 | **17969**